*J Mater Sci* (2018) 53:4294–4305

Electronic materials

# Theoretical study of phase stability, crystal and electronic structure of $MeMgN_2$ (Me = Ti, Zr, Hf) compounds

M. A. Gharavi[1,*], R. Armiento[2], B. Alling[2,3], and P. Eklund[1]

[1] Thin Film Physics Division, Department of Physics, Chemistry and Biology (IFM), Linköping University, 581 83 Linköping, Sweden
[2] Theory and Modelling Division, Department of Physics, Chemistry and Biology (IFM), Linköping University, 581 83 Linköping, Sweden
[3] Max-Planck-Institut für Eisenforschung GmbH, 40237 Düsseldorf, Germany

**Received:** 6 July 2017
**Accepted:** 21 November 2017
**Published online:** 30 November 2017



## ABSTRACT

Scandium nitride has recently gained interest as a prospective compound for thermoelectric applications due to its high Seebeck coefficient. However, ScN also has a relatively high thermal conductivity, which limits its thermoelectric efficiency and figure of merit ($zT$). These properties motivate a search for other semiconductor materials that share the electronic structure features of ScN, but which have a lower thermal conductivity. Thus, the focus of our study is to predict the existence and stability of such materials among inherently layered equivalent ternaries that incorporate heavier atoms for enhanced phonon scattering and to calculate their thermoelectric properties. Using density functional theory calculations, the phase stability of $TiMgN_2$, $ZrMgN_2$ and $HfMgN_2$ compounds has been calculated. From the computationally predicted phase diagrams for these materials, we conclude that all three compounds are stable in these stoichiometries. The stable compounds may have one of two competing crystal structures: a monoclinic structure ($LiUN_2$ prototype) or a trigonal superstructure ($NaCrS_2$ prototype; $R\bar{3}mH$). The band structure for the two competing structures for each ternary is also calculated and predicts semiconducting behavior for all three compounds in the $NaCrS_2$ crystal structure with an indirect band gap and semiconducting behavior for $ZrMgN_2$ and $HfMgN_2$ in the monoclinic crystal structure with a direct band gap. Seebeck coefficient and power factors are also predicted, showing that all three compounds in both the $NaCrS_2$ and the $LiUN_2$ structures have large Seebeck coefficients. The predicted stability of these compounds suggests that they can be synthesized by, e.g., physical vapor deposition.

Address correspondence to E-mail: mohammad.amin.gharavi@liu.se



https://doi.org/10.1007/s10853-017-1849-0

## Introduction

Thermoelectric materials and devices, which directly convert a thermal gradient into an external voltage, are reliable and low-maintenance power-generating materials used for niche applications such as solid-state cooling or electric power supplying units in deep-space exploration. However, the use of thermoelectrics is presently limited [1] by their low efficiency and high cost. For example, the crustal abundance and global production of tellurium is low [2, 3]. This limits widespread use of the benchmark thermoelectric materials ($Bi_2Te_3$ and PbTe). Thus, there is a need for replacement materials.

The thermoelectric efficiency is directly connected to the dimensionless figure of merit:

$$zT = \left(\frac{S^2\sigma}{\kappa}\right) \times T,$$

where $S$ is the Seebeck coefficient, $\sigma$ is the electrical conductivity, $\kappa$ is the thermal conductivity, and $T$ is the absolute temperature [4]. The product $S^2\sigma$ is known as the power factor. In the limit of $zT \to \infty$, the Carnot engine efficiency (i.e., the maximum efficiency achievable in a heat engine) is obtained. However, designing materials with higher $zT$ values is a difficult challenge, as all three terms are interrelated in a way that typically limits $zT$ to below unity in commonly available materials.

In order to overcome this barrier, Slack proposed the phonon glass–electron crystal (PGEC) approach for thermoelectric material design [5–7]: one should seek a material with a high Seebeck coefficient value and engineer it in such a way that it will behave like a crystal for electrons, but scatter phonons similarly to glass. As a result, added material optimization processes are required to increase the $zT$ of any given material.

As a starting point for this approach of engineering a high $zT$ material, prior works have suggested cubic scandium nitride (ScN) [8]. The Seebeck coefficient of ScN is relatively large (reaching $-$ 180 μV/K at 800 K) and because of its low electrical resistivity, large power factors between 2.5 and 3.5 $\times$ $10^{-3}$ $Wm^{-1}K^{-2}$ have been reported [9, 10]. Doping and alloying ScN with heavy elements [11, 12] and/or creating artificial layer interfaces such as metal/semiconductor superlattices [13–16] can alter properties and decrease the thermal conductivity, resulting in an enhanced $zT$. Furthermore, ScN can also become $p$-type by Sc-site doping [17, 18]. Although the direction of research is promising, ScN does have a relatively large thermal conductivity [19–22] of approximately 8–12 $Wm^{-1}K^{-1}$. Scandium and nitrogen are both light atoms compared to their heavier counterparts such as lead, bismuth and tellurium which effectively scatter phonons [23], and artificial interfaces seen in superlattices are synthesized at a sub micrometer scale, while thermoelectric power generation requires millimeter-sized bulk samples [24]. Also, scandium does not have phonon isotope scattering as it is an isotopically pure element.

In a recent paper, Alling [25] addressed these issues by proposing an equivalent ternary based on ScN. Scandium (which is a group-3 element) can be replaced with one group-2 and one group-4 element in a 50/50 proportion to cover the same electron valence. The final compound should then have a $MeAEN_2$ stoichiometry, with Me representing a transition metal from the group-4 elements and $AE$ belonging to the group-2 (alkaline earth) elements, such as magnesium. $TiMgN_2$ was predicted to be stable using density functional theory (DFT). Band structure calculations predicted stoichiometric $TiMgN_2$ to have a 1.11 eV band gap using the HSE06 [25, 26] hybrid functional. This methodology has also been used by Tholander et al. [27] to predict zinc-based group-4 transition metal nitride stability and crystal structure. While much research has been done regarding Ti–Si–N [28–30] and Ti–Al–N [31–34] which show superior hardness and/or oxidization resistance compared to TiN, there are much fewer studies reported for Ti–Mg–N [35–39]. $TiMgN_2$ may crystallize in the B1–$L1_1$ superstructure [25], which could open a new opportunity for hard coating research by inter-layer dissipation of heat or research for hard coatings with better mechanical properties.

In this paper, we continue the work in investigating ternary structures based on ScN. We also computationally study the phase stability, band structure, Seebeck coefficient and power factor of two more candidate compounds potentially useful in thermoelectric applications, $ZrMgN_2$ and $HfMgN_2$. As Ti, Zr and Hf belong to group 4 of the periodic table, all three share similar physical and chemical properties, and it can be assumed that any stable Ti-based ternary may also exist for Zr and Hf.

## Computational details

Over 60 different and chemically stoichiometric crystal structures registered in the Inorganic Crystal Structure Database (ICSD) [40] were studied in order to calculate the formation enthalpy of Ti–Mg–N, Zr–Mg–N and Hf–Mg–N and prepare the necessary phase diagrams. Although the binary nitrides are well known, $TiMgN_2$, $ZrMgN_2$ and $HfMgN_2$ are not present in either the Materials Project database [41] or the ICSD. Half of these crystal structures follow the $MeMgN_2$ stoichiometry, while the remaining crystal structures belong to various Mg-, Ti-, Zr- and Hf-based ternaries. In addition, the opposite sequence, $MgMeN_2$, was also studied in case some structures would show a different phase when switching the positions of the metal atoms in their respective sublattice.

First-principles calculations were employed using DFT [42, 43] with the projector augmented wave method (PAW) [44] implemented in the Vienna ab initio simulation package (VASP) [45–47] version 5.2. Electronic exchange correlation effects and the electronic band structure were modeled with the generalized gradient approximation (GGA) using Perdew–Burke–Ernzerhof (PBE) functional [48]. It should be noted that the Kohn–Sham gaps of standard GGA calculations are systematically smaller than experimental band gaps, but for the present work this is not an issue since we are mostly concerned with dismissing metallic compositions. To the extent that we identify relevant compounds, they can be further investigated by in-depth theoretical work and/or by laboratory synthesis of the three ternary nitrides. The plane wave energy cutoff was set at 400 eV. The required structure files for the crystal structures were obtained from the ICSD and converted to VASP input files using cif2cell [49]. Phase diagrams were prepared using the software package Pymatgen (Python Materials Genomics) [50], the band structure illustrations by the high-throughput toolkit (httk) [51] and the crystal structures by VESTA [52]. For the phase diagrams, the formation energy per atom was calculated for each ternary compound and related to competing ternary stoichiometries and neighboring binary compounds. The Materials Project database provided the formation enthalpies of all of the binaries (TiN, ZrN, HfN, $Mg_3N_2$, etc.).

The present work uses the same correction of the $N_2$ energy as used in the Materials Project, based on work by Wang et al. [53] as standard GGA exchange–correlation functionals in DFT are known to, in general, have systematic errors in the prediction of energy differences between solid and gas phase systems [54]. Hence, to accurately reproduce the formation energy of a system relative to a gas end point, it is common to adjust the gas phase energy.

The calculations used an $11 \times 11 \times 11$ $k$-point mesh for Brillouin zone sampling and were executed with the Monkhorst–Pack scheme [55]. For band structure calculations, the tetrahedron method was used in order to obtain band gap values with spin polarization included [56].

Finally, the Seebeck coefficient $S$ and power factor $S^2\sigma\tau^{-1}$ (being the charge carrier relaxation time) of the predicted semiconductors is calculated at room temperature and 600 K as functions of the chemical potential using Boltzmann transport theory with the constant relaxation time approximation. We use the software BoltzTraP [57] on DFT calculations with a $40 \times 40 \times 40$ $k$-point mesh for Brillouin zone sampling.

## Results

### $TiMgN_2$

Figure 1a shows the phase diagram for Ti–Mg–N. Although 28 different crystal structures other than those that follow the $MeMgN_2$ formula (such as $Ca_4TiN_4$ [58], perovskite $CaTiO_3$ [59], $Ti_2AlN$ and $Ti_4AlN_3$ MAX-phases [60]) were tested, only the ordered $TiMgN_2$ stoichiometry is found to be thermodynamically stable relative to known and investigated phases with the other ordered stoichiometries being either unstable or metastable. Random $Ti_{1-x}Mg_xN$ solid solutions with the rocksalt structure have, however, been found to be thermodynamically stable for a range of compositions [25]. This precise stoichiometry occurred in 29 of the investigated crystal structures. These include the trigonal $NaCrS_2$ ($R\bar{3}mH$) superstructure [61], the tetragonal $BaNiS_2$ ($P4/n\ m\ m\ Z$) superstructure [62], tetragonal $LiUN_2$ [63], $ZnGeN_2$ [64] (based on the $NaFeO_2$-beta structure) and the inverse-MAX $BaCeN_2$ [65].

In order to differentiate between these structures, Table 1 lists a selected group of examples with their respective formation enthalpies. These results show that crystallization into the $NaCrS_2$ is the most likely

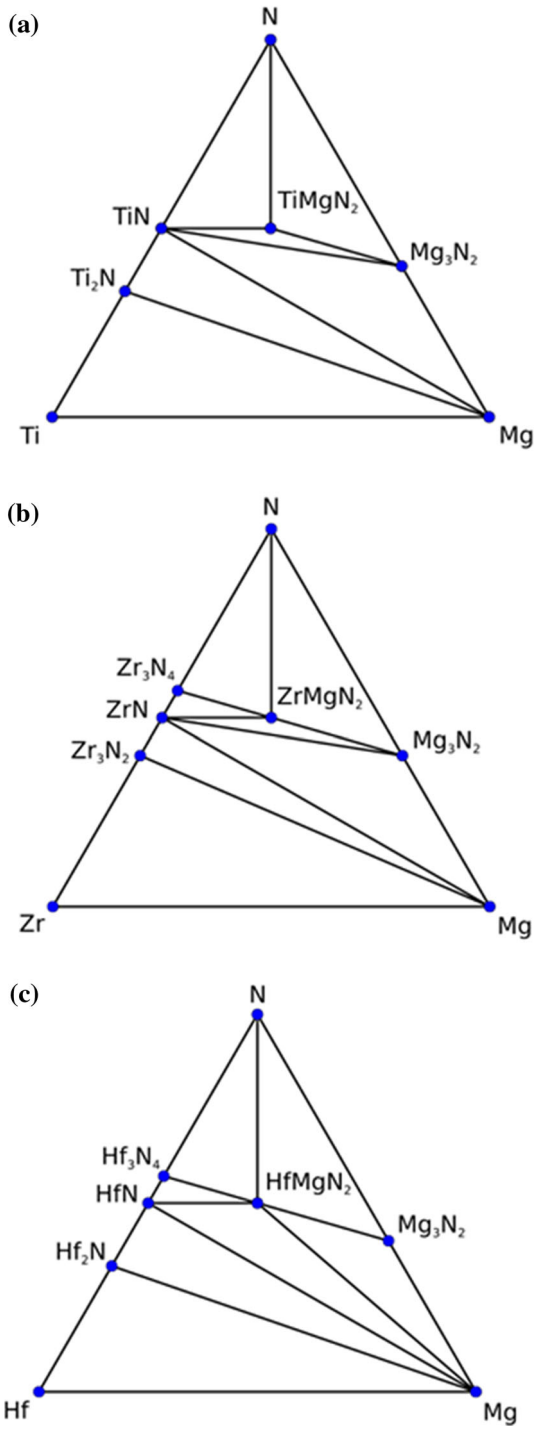


**Figure 1** Phase diagram for **a** Ti–Mg–N, **b** Zr–Mg–N and **c** Hf–Mg–N. Only predicted stable structures located on the convex hull are shown. Only the $MeMgN_2$ stoichiometry is predicted to be stable.

outcome with a − 1.299 eV formation enthalpy and a 0.04 eV difference compared to the $LiUN_2$ structure which agrees with the findings mentioned in Ref. [25]. It should be noted that the difference between the formation enthalpies of these two crystal structures would most likely mean that $NaCrS_2$ is the preferred structure, but $LiUN_2$ is also studied for any comparison needed between $TiMgN_2$, $ZrMgN_2$ and $HfMgN_2$.

Both crystal structures are shown in Fig. 2. The results suggest that $TiMgN_2$ will crystallize into the $NaCrS_2$ superstructure (also viewed as a NaCl-B1 superstructure that includes three alternating layers of Ti and Mg) which could cause phonon scattering at the interface of each layer as mentioned in the introduction. Figure 3a, d shows the band structures for $TiMgN_2$ in the $NaCrS_2$ and $LiUN_2$ structures. According to these results, $TiMgN_2$ is a semiconductor with a Kohn–Sham PBE band gap of 0.26 eV in the $NaCrS_2$ structure (Fig. 3a). However, the case for $LiUN_2$ (Fig. 3d) is different, as band structure calculations show no band gap, i.e., predicting metallic properties. It is possible that $TiMgN_2$ could crystallize in the $LiUN_2$ structure as a metastable phase. Table 2 shows the lattice parameters and the band gap energy in both crystal structures. These results show that although the trigonal $NaCrS_2$ crystal structure remains with only the lattice parameters changing, the $LiUN_2$ structure relaxes from tetragonal to monoclinic according to the calculated unit cell lattice parameters.

Figure 4a, b shows the Seebeck coefficient of $TiMgN_2$ versus the chemical potential at room temperature and 600 K, respectively. Only the $NaCrS_2$ structure was studied as the $LiUN_2$ structure was predicted with no band gap. These results show relatively high Seebeck coefficient values at the Fermi level. Figure 5a, b shows $(S^2\sigma)/\tau$ versus the chemical potential at room temperature and 600 K, respectively. Depending on the assumed relaxation time, predicted power factor values could exceed those of ScN (Fig. 5k, l).

## $ZrMgN_2$

Figure 1b shows the phase diagram for $ZrMgN_2$. Also here the only stable ternary has the $MeMgN_2$ stoichiometry. As for the preferred crystal structure, formation enthalpies for the selected crystal structures are shown in Table 3. In contrast to $TiMgN_2$, the $LiUN_2$ structure competes with the $NaCrS_2$ structure with less than 0.01 eV formation enthalpy difference.

**Table 1** Formation enthalpies for $TiMgN_2$ crystallized in five different structures

| $TiMgN_2$ | | |
|---|---|---|
| ICSD id | Formation enthalpy (eV/atom) | Nitride example |
| 82537 | − 1.299 | $SrZrN_2$ ($NaCrS_2$) |
| 98663 | − 1.260 | $LiUN_2$ |
| 74904 | − 1.005 | $BaZrN_2$ ($BaNiS_2$) |
| 15144 | − 1.234 | $ZnGeN_2$ ($NaFeO_2$-beta) |
| 74791 | − 1.222 | $BaCeN_2$, inverse-MAX |

The ICSD id is the entry identification number which the structure is based on. The nitride examples represent actual existing ternary compounds and the respective structures which they crystallize in

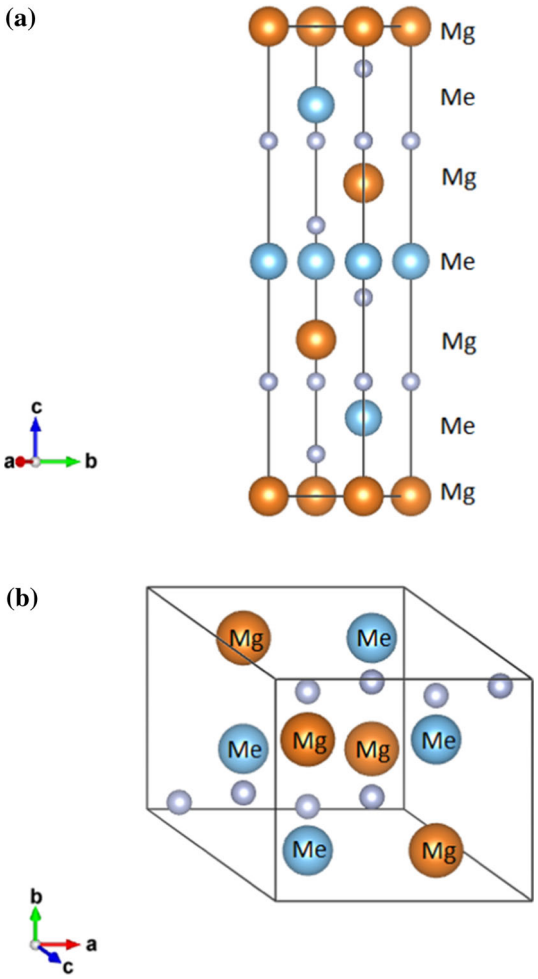


**Figure 2** 3D visualization of *Me*$MgN_2$ crystallized into: **a** the $NaCrS_2$ (trigonal unit cell) and **b** the $LiUN_2$ (relaxed monoclinic unit cell) structure.

The predicted band structures are shown in Fig. 3b, e. In both cases, $ZrMgN_2$ is a semiconductor regardless of crystal structure. However, for the $NaCrS_2$ crystal structure we find an indirect Kohn–Sham PBE band gap of 0.89 eV and for the $LiUN_2$ structure, a direct band gap of 0.46 eV. The respective lattice parameters and band gap energy are shown in Table 4. $ZrMgN_2$ relaxes in a similar way as $TiMgN_2$ with the $NaCrS_2$ structure remaining the same while the tetragonal $LiUN_2$ structure relaxes into a monoclinic structure according to the calculated unit cell lattice parameters.

Figure 4b, g (room-temperature calculations) and Fig. 4d, h (600 K calculations) shows the Seebeck coefficient of $ZrMgN_2$ versus the chemical potential in the $NaCrS_2$ and the $LiUN_2$ structures. These results show an increase in the Seebeck coefficient values and a slight shift in the chemical potential compared to $TiMgN_2$ with higher values seen in the $NaCrS_2$ structure. Figure 5b, g and d, h shows the $(S^2\sigma)/\tau$ versus chemical potential at room temperature and 600 K, respectively. These results predict power factor values close to the Fermi level which are larger than those of ScN (Fig. 5k, l).

## $HfMgN_2$

Figure 1c shows the phase diagram for Hf–Mg–N. Similar to both $TiMgN_2$ and $ZrHfN_2$, the $HfMgN_2$ stoichiometry is predicted to be stable. Table 5 compares a selected group of crystal structures and shows the $NaCrS_2$ and $LiUN_2$ structures with similar formation enthalpies (less than 0.01 eV difference), thus predicting a competition between the two structures.

Figure 3c, f shows the predicted band structures for both $NaCrS_2$ and $LiUN_2$. Similar to $ZrMgN_2$, an indirect band gap of 1.19 eV is predicted for the $NaCrS_2$ structure, while a 0.77 eV direct band gap is predicted for the $LiUN_2$ structure. The respective lattice parameters and band gap energies are shown in Table 6. Similar to $TiMgN_2$ and $ZrMgN_2$, $HfMgN_2$

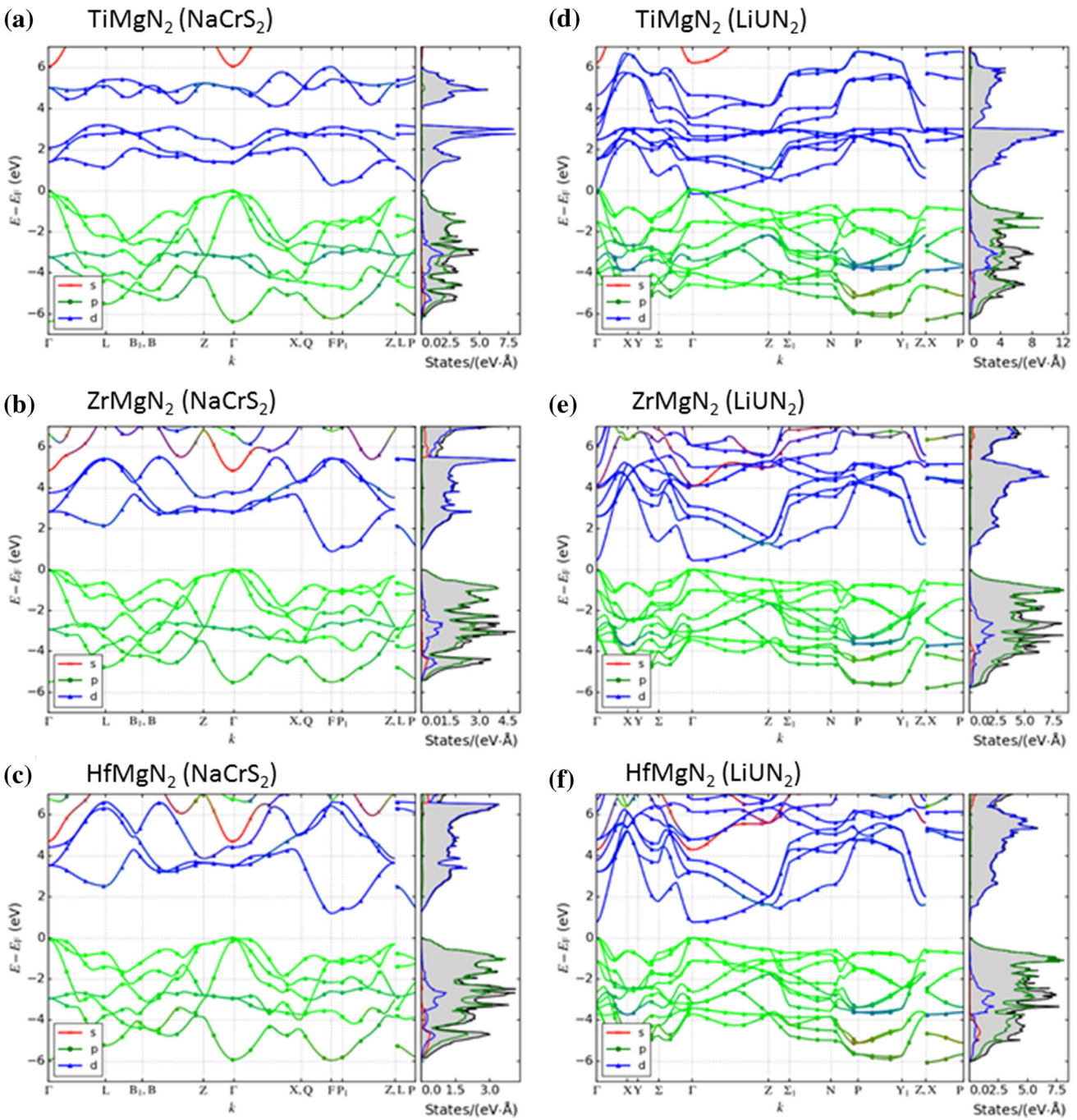


**Figure 3** Band structure of **a** $TiMgN_2$, **b** $ZrMgN_2$ and **c** $HfMgN_2$ for the $NaCrS_2$ structure (left column) predicting an indirect band gap for all three compounds. Band structure of **d** $TiMgN_2$, **e** $ZrMgN_2$ and **f** $HfMgN_2$ for the $LiUN_2$ structure (right column) predicting a direct band gap for $ZrMgN_2$ and $HfMgN_2$. Note: s, p and d indicate the relative contributions to the total sum, s + p + d, not the absolute projected values.

preserves the trigonal $NaCrS_2$ structure but relaxes from tetragonal $LiUN_2$ into a monoclinic structure.

Figure 4e, i (room-temperature calculations) and Fig. 4f, j (600 K calculations) shows the Seebeck coefficient of $HfMgN_2$ versus the chemical potential in the $NaCrS_2$ and the $LiUN_2$ structures. These results show an increase in the Seebeck coefficient values and a larger shift in the chemical potential compared

**Table 2** Lattice parameters, unit cell volumes and band gap values for $TiMgN_2$ crystallized in both $NaCrS_2$ and $LiUN_2$

| Crystal structure | Compound ($MeMgN_2$) | $a$ (Å) | $b$ (Å) | $c$ (Å) | Volume (Å$^3$) | Band gap (eV) |
|---|---|---|---|---|---|---|
| $NaCrS_2$ (trigonal) | $TiMgN_2$ | 2.9997 $\alpha = 90°$ | 2.9997 $\beta = 90°$ | 14.8838 $\gamma = 120°$ | 115.9849 | Indirect: 0.26 |
| $LiUN_2$ (tetragonal relaxed into monoclinic) | $TiMgN_2$ | 5.9777 $\alpha = 90°$ | 5.9777 $\beta =$ 55.1530° | 5.2309 $\gamma = 90°$ | 153.3962 | No gap: metallic? |

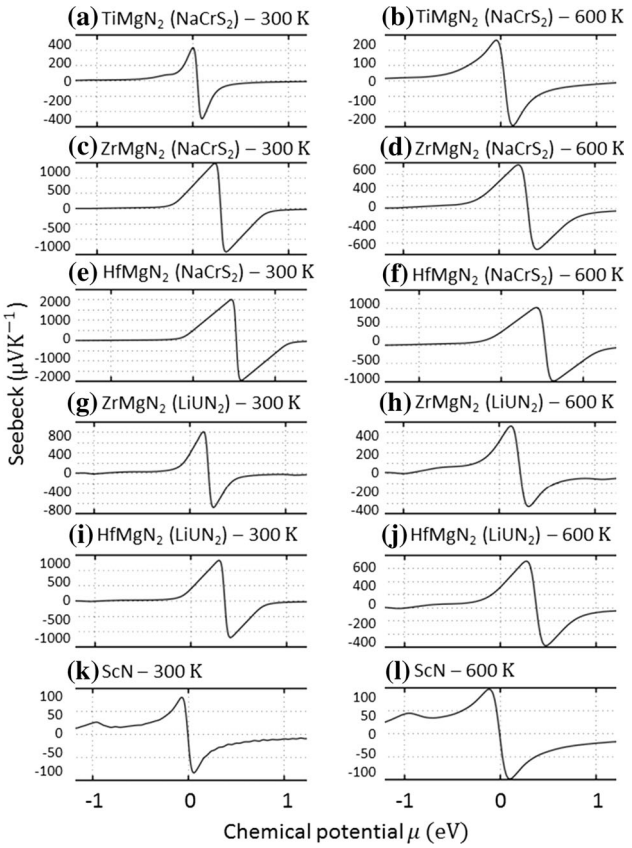


**Figure 4** Seebeck coefficient value versus chemical potential of **a** $TiMgN_2$, **b** $ZrMgN_2$ and **c** $HfMgN_2$ for the $NaCrS_2$ and $LiUN_2$ structures at room temperature and 600 K. The Seebeck coefficient value of ScN is also added for comparison.

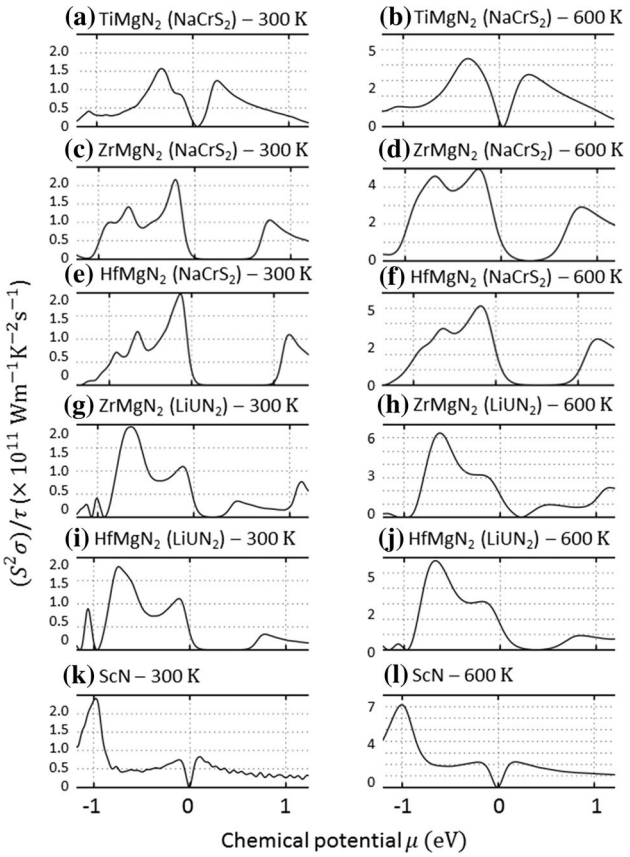


**Figure 5** $(S^2\sigma)/\tau$ value versus chemical potential of **a** $TiMgN_2$, **b** $ZrMgN_2$ and **c** $HfMgN_2$ for the $NaCrS_2$ and $LiUN_2$ structures at room temperature and 600 K. The $(S^2\sigma)/\tau$ value of ScN is also added for comparison.

to both $TiMgN_2$ and $ZrMgN_2$ with higher values seen in the $NaCrS_2$ structure. Figure 5e, i and f, j shows the $(S^2\sigma)/\tau$ versus chemical potential at room temperature and 600 K, respectively. These results predict power factor values almost equal to those of $ZrMgN_2$ and larger than that of ScN close to the Fermi level (Fig. 5k, l).

## Discussion

For $ZrMgN_2$ and $HfMgN_2$, the formation enthalpies of the $NaCrS_2$ and the $LiUN_2$ structure are close, within the accuracy of our approach. This suggests that both of these structures may be possible to synthesize, i.e., with the one higher in energy as a long-lasting metastable state. The shifting between the $NaCrS_2$ and the $LiUN_2$ structures could be done by

**Table 3** Formation enthalpies for $ZrMgN_2$ crystallized in five different structures

| $ZrMgN_2$ | | |
|---|---|---|
| ICSD id | Formation enthalpy (eV/atom) | Nitride example |
| 82537 | − 1.307 | $SrZrN_2$ ($NaCrS_2$) |
| 98663 | − 1.311 | $LiUN_2$ |
| 74904 | − 0.897 | $BaZrN_2$ ($BaNiS_2$) |
| 15144 | − 1.230 | $ZnGeN_2$ ($NaFeO_2$-beta) |
| 74791 | − 1.223 | $BaCeN_2$, inverse-MAX |

**Table 4** Lattice parameters, unit cell volumes and band gap values for $ZrMgN_2$ crystallized in both $NaCrS_2$ and $LiUN_2$

| Crystal structure | Compound ($MeMgN_2$) | $a$ (Å) | $b$ (Å) | $c$ (Å) | Volume (Å$^3$) | Band gap (eV) |
|---|---|---|---|---|---|---|
| $NaCrS_2$ (trigonal) | $ZrMgN_2$ | 3.2077 $\alpha = 90°$ | 3.2077 $\beta = 90°$ | 15.3237 $\gamma = 120°$ | 136.5495 | Indirect: 0.89 |
| $LiUN_2$ (tetragonal relaxed into monoclinic) | $ZrMgN_2$ | 6.3113 $\alpha = 90°$ | 6.3113 $\beta = 55.3470°$ | 5.5498 $\gamma = 90°$ | 181.8447 | Direct: 0.46 |

**Table 5** Formation enthalpies for $HfMgN_2$ crystallized in five different structures

| $HfMgN_2$ | | |
|---|---|---|
| ICSD id | Formation enthalpy (eV/atom) | Nitride example |
| 82537 | − 1.447 | $SrZrN_2$ ($NaCrS_2$) |
| 98663 | − 1.453 | $LiUN_2$ |
| 74904 | − 1.034 | $BaZrN_2$ ($BaNiS_2$) |
| 15144 | − 1.360 | $ZnGeN_2$ ($NaFeO_2$-beta) |
| 74791 | − 1.362 | $BaCeN_2$, inverse-MAX |

**Table 6** Lattice parameters, unit cell volumes and band gap values for $HfMgN_2$ crystallized in both $NaCrS_2$ and $LiUN_2$

| Crystal structure | Compound ($MeMgN_2$) | $a$ (Å) | $b$ (Å) | $c$ (Å) | Volume (Å$^3$) | Band gap (eV) |
|---|---|---|---|---|---|---|
| $NaCrS_2$ (trigonal) | $HfMgN_2$ | 3.1679 $\alpha = 90°$ | 3.1679 $\beta = 90°$ | 15.2463 $\gamma = 120°$ | 132.5114 | Indirect: 1.19 |
| $LiUN_2$ (tetragonal relaxed into monoclinic) | $HfMgN_2$ | 6.2300 $\alpha = 90°$ | 6.2300 $\beta = 55.5036°$ | 5.5001 $\gamma = 90°$ | 175.9362 | Direct: 0.77 |

choosing suitable substrates for epitaxial stabilization during the synthesis process. Despite that we cannot with certainty determine which of the structures for $ZrMgN_2$ and $HfMgN_2$ are thermodynamically stable, both are semiconductors. This motivates future studies on synthesis for thermoelectrics and other applications. It should be noted that the $NaCrS_2$ structures show indirect band gaps with larger values and large slopes for the density of states at the Fermi level compared to their direct band gap counterparts in the $LiUN_2$ structure. Another feature seen in all three compounds is the relation between band gap values and lattice parameters with the transition metal, *Me*. As the smaller Ti atom is replaced with the larger Zr atom, the lattice parameters, cell volume and band gap value increase, which is expected. However, only the band gap value increases when Zr is replaced with Hf as the *f* orbital electrons are not effective at screening the increasing charge, resulting in similar atomic size (lanthanide contraction [66]) and similar lattice parameters.

Although the present results are promising, actual attempts to synthesize these prospective compounds would be important. Similar to the synthesis of MAX-phase [67] thin films, it should be possible to synthesize ordered $TiMgN_2$, $ZrMgN_2$ and $HfMgN_2$ outside thermodynamic equilibrium in a magnetron sputtering system. All of the mentioned elements are vacuum compatible, and one could use the deposition parameters needed for stoichiometric TiN, ZrN, HfN and $Mg_3N_2$ to reach a Me/Mg $= 1$ ratio and fine-tune the $MeMgN_2$ stoichiometry. References [36, 38] note the deposition temperature for rocksalt (Ti, Mg)N alloys to be between 200 and 300 °C with oxidization resistance close to 700 °C (suitable for mid-temperature thermoelectric applications). If the layered $NaCrS_2$ superstructure is preferred, it would be advisable to use either high-temperature direct growth or low-temperature deposition, followed by high-temperature annealing [68] (in ammonia or nitrogen). In this case, GaN or SiC [69] substrates could be considered for their suitable lattice constant and thermal stability.

As for the thermoelectric properties, the calculated Seebeck coefficient values show that in the range of a moderate change in the Fermi level, high room-temperature Seebeck coefficient values can be achieved (Fig. 4), although it seems that $HfMgN_2$ is either an insulator or would require elemental doping due to the larger shift in the chemical potential.

Note that what we have calculated is the power factor divided by the relaxation time. The results (Fig. 5) can be used as an estimate of the difference in thermoelectric performance at various doping levels between the studied compounds and known materials, e.g., ScN, as shown for comparison in Figs. 4k, l and 5k, l. However, such a comparison is made under the assumptions that the constant relaxation time approximation holds sufficiently well and that the relaxation time for the compounds is similar. For more precise predictions, the relaxation time value needs to be obtained from experimental data, as it can for example for common thermoelectric materials such as $Bi_2Te_3$ [70, 71].

As ordered $TiMgN_2$, $ZrMgN_2$ and $HfMgN_2$ have not yet been studied experimentally, such data do not exist, and obtaining meaningful numbers for the electrical conductivity is difficult. However, using experimental data from Burmistrova et al. [19] and the classical equation for conductivity ($\sigma = ne^2\tau m^{-1}$), the constant relaxation time $\tau$ for ScN (which the ternaries were modeled after) is estimated to be equal to $6.5 \times 10^{-14}$ s.

## Conclusions

Theoretical methods were used to study the phase stability and band structure of $TiMgN_2$, $ZrMgN_2$ and $HfMgN_2$. In all three cases, only $MeMgN_2$ is predicted to be the stable stoichiometry. It is shown that stoichiometric $TiMgN_2$ crystallizes into the hexagonal $NaCrS_2$ superstructure with a 0.26 eV indirect Kohn–Sham PBE band gap. $ZrMgN_2$ and $HfMgN_2$ were also studied, which shows tendency to crystallize in both the $NaCrS_2$ superstructure and the $LiUN_2$ prototype monoclinic structure. Both show semiconducting properties regardless of the crystal structure. $ZrMgN_2$ shows a 0.89 eV indirect band gap when crystallizing into the $NaCrS_2$ structure, while as crystallization into the $LiUN_2$ structure results in a 0.46 eV direct band gap. As for $HfMgN_2$, the band gap increases as crystallization into $NaCrS_2$ results in a 1.19 eV indirect band gap and crystallization into $LiUN_2$ results in a 0.77 eV direct band gap. Lattice parameters and cell volumes increase with the substitution of Ti with Zr, but slightly decrease when Zr is substituted with Hf.

Finally, the Seebeck coefficient and power factor was calculated for all of the semiconducting compounds. The results show that in the range of a moderate change in the Fermi level, high room-temperature Seebeck coefficient values can be achieved.

Thus, the predicted stability and semiconducting properties of these compounds can be further studied both theoretically and experimentally for any prospective thermoelectric properties.

## Acknowledgements

The authors acknowledge funding from the European Research Council under the European Community's Seventh Framework Programme (FP/2007-2013)/ERC Grant Agreement No. 335383, the Swedish Government Strategic Research Area in Materials Science on Functional Materials at Linköping University (Faculty Grant SFO-Mat-LiU No. 2009 00971), the Swedish Foundation for Strategic Research (SSF) through the Future Research Leaders

5 and 6 programs, the Knut and Alice Wallenberg foundation through the Academy Fellow program and the Swedish Research Council (VR) under Project Nos. 621-2012-4430 and 2016-03365. Financial support by the Swedish Research Council (VR) through International Career Grant No. 330-2014-6336 and Marie Sklodowska Curie Actions, Cofund, Project INCA 600398, is gratefully acknowledged. Financial support from VR Grant No. 2016-04810 and the Swedish e-Science Research Centre (SeRC) is also acknowledged. The authors also wish to thank the Swedish National Infrastructure for Computing (SNIC) which provided access to the necessary supercomputer resources located at the National Supercomputer Center (NSC).



## References

[1] Yang J, Caillat T (2006) Thermoelectric materials for space and automotive power generation. MRS Bull 31:224–229

[2] Brown TJ (2011) World mineral statistics: British Geological Survey. Keyworth, Nottingham

[3] Amatya R, Ram RJ (2012) Trend for thermoelectric materials and their earth abundance. J Electr Mater 41:1011

[4] Goldsmid HJ (2010) Introduction to thermoelectricity. Springer, Berlin

[5] Rowe DM (1995) CRC handbook of thermoelectrics. CRC Press LLC, Boca Raton, pp 399–432

[6] Tritt TM (2011) Thermoelectric phenomena, materials, and applications. Annu Rev Mater Res 41:433–448

[7] Shakouri A (2011) Recent developments in semiconductor thermoelectric physics and materials. Annu Rev Mater Res 41:399–431

[8] Eklund P, Kerdsongpanya S, Alling B (2016) Transition-metal-nitride-based thin films as novel energy harvesting materials. J Mater Chem C 4:3905–3914

[9] Kerdsongpanya S, Nong NV, Pryds N, Žukauskaitė A, Jensen J, Birch J, Lu J, Hultman L, Wingqvist G, Eklund P (2011) Anomalously high thermoelectric power factor in epitaxial ScN thin films. Appl Phys Lett 99:232113

[10] Burmistrova PV, Zakharov DN, Favaloro T, Mohammed A, Stach EA, Shakouri A, Sands TD (2015) Effect of deposition pressure on the microstructure and thermoelectric properties of epitaxial ScN(001) thin films sputtered onto MgO(001) substrates. J Mater Res 30:626–634

[11] Kerdsongpanya S, Alling B, Eklund P (2013) Phase stability of ScN-based solid solutions for thermoelectric applications from first-principles calculations. J Appl Phys 114:073512

[12] Tureson N, Nong NV, Fournier D, Singh N, Acharya S, Schmidt S, Belliard L, Soni A, le Febvrier A, Eklund P (2017) Reduction of the thermal conductivity of the thermoelectric material ScN by Nb alloying. J Appl Phys 122:025116

[13] Schroeder JL, Ewoldt DA, Amatya R, Ram RJ, Shakouri A, Sands TD (2014) Bulk-like laminated nitride metal/semiconductor superlattices for thermoelectric devices. J Microelectromech Syst 23:672–680

[14] Saha B, Koh YR, Comparan J, Sadasivam S, Schroeder JL, Garbrecht M, Mohammed A, Birch J, Fisher T, Shakouri A, Sands TD (2016) Cross-plane thermal conductivity of (Ti, W)N/(Al, Sc)N metal/semiconductor superlattices. Phys Rev B 93:045311

[15] Rawat V, Koh YK, Cahill DG, Sands TD (2009) Thermal conductivity of (Zr, W) N/ScN metal/semiconductor multilayers and superlattices. J Appl Phys 105:024909

[16] Saha B, Koh YR, Feser JP, Sadasivam S, Fisher TS, Shakouri A, Sands TD (2017) Phonon wave effects in the thermal transport of epitaxial TiN/(Al, Sc)N metal/semiconductor superlattices. J Appl Phys 121:015109

[17] Saha B, Naik G, Drachev V, Boltasseva A, Marinero EE, Sands TD (2013) Electronic and optical properties of ScN and (Sc, Mn)N thin films deposited by reactive DC-magnetron sputtering. J Appl Phys 114:063519

[18] Saha B, Garbrecht M, Perez-Taborda JA, Fawey MH, Koh YR, Shakouri A, Martin-Gonzalez M, Hultman L, Sands TD (2017) Compensation of native donor doping in ScN: carrier concentration control and p-type ScN. Appl Phys Lett 110:252104

[19] Burmistrova PV, Maassen J, Favaloro T, Saha B, Salamat S, Koh YR, Lundstrom MS, Shakouri A, Sands TD (2013) Thermoelectric properties of epitaxial ScN films deposited by reactive magnetron sputtering onto MgO(001) substrates. J Appl Phys 113:153704

[20] King SW, Davis RF, Nemanich RJ (2014) Gas source molecular beam epitaxy of scandium nitride on silicon carbide and gallium nitride surfaces. J Vac Sci Technol, A 32:061504

[21] Kerdsongpanya S, Sun B, Eriksson F, Jensen J, Lu J, Koh YK, Nong NV, Balke B, Alling B, Eklund P (2016)

Experimental and theoretical investigation of $Cr_{1-x}Sc_xN$ solid solutions for thermoelectrics. J Appl Phys 120:215103

[22] Kerdsongpanya S, Hellman O, Sun B, Koh YK, Lu J, Nong NV, Simak SI, Alling B, Eklund P (2017) Phonon thermal conductivity of scandium nitride for thermoelectrics from first-principles calculations and thin-film growth. Phys Rev B 96:195417

[23] DiSalvo FJ (1999) Thermoelectric cooling and power generation. Science 285:703–706

[24] Schroeder JL (2012) (Hafnium zirconium) nitride/scandium nitride metal/semiconductor superlattices for thermionic energy conversion, PhD Dissertation, Purdue University

[25] Alling B (2014) Metal to semiconductor transition and phase stability of $Ti_{1-x}Mg_xN_y$ alloys investigated by first-principles calculations. Phys Rev B 89:085112

[26] Heyd J, Scuseria GE, Ernzerhof M (2003) Hybrid functionals based on a screened Coulomb potential. J Chem Phys 118:8207–8215

[27] Tholander C, Andersson CBA, Armiento R, Tasnádi F, Alling B (2016) Strong piezoelectric response in stable $TiZnN_2$, $ZrZnN_2$, and $HfZnN_2$ found by ab initio high-throughput approach. J Appl Phys 120:225102

[28] Hao S, Delley B, Stampfl C (2006) Structure and properties of TiN(111)/$Si_xN_y$/TiN (111) interfaces in superhard nanocomposites: first-principles investigations. Phys Rev B 74:035402

[29] Hultman L, Bareno J, Flink A, Söderberg H, Larsson K, Petrova V, Oden M, Greene JE, Petrov I (2007) Interface structure in superhard TiN-SiN nanolaminates and nanocomposites: film growth experiments and ab initio calculations. Phys Rev B 75:155437

[30] Zhang RF, Veprek S (2007) Crystalline-to-amorphous transition in $Ti_{1-x}Si_xN$ solid solution and the stability of fcc SiN studied by combined ab initio density functional theory and thermodynamic calculations. Phys Rev B 76:174105

[31] Hörling A, Hultman L, Oden M, Sjölen J, Karlsson L (2002) Thermal stability of arc evaporated high aluminum-content $Ti_{1-x}Al_xN$ thin films. J Vac Sci Technol A 20:1815–1823

[32] McIntyre D, Greene JE, Håkansson G, Sundgren J-E, Münz W-D (1990) Oxidation of metastable single-phase polycrystalline $Ti_{0.5}Al_{0.5}N$ films: kinetics and mechanisms. J Appl Phys 67:1542–1553

[33] Mayrhofer PH, Hörling A, Karlsson L, Sjölén J, Larsson T, Mitterer C, Hultman L (2003) Self-organized nanostructures in the Ti–Al–N system. Appl Phys Lett 83:2049–2051

[34] Hörling A, Hultman L, Odén M, Sjölén J, Karlsson L (2005) Mechanical properties and machining performance of $Ti_{1-x}Al_xN$-coated cutting tools. Surf Coat Technol 191:384–392

[35] Banakh O, Balzer M, Fenker M, Blatter A (2004) Spectroellipsometric evaluation of colour and oxidation resistance of TiMgN coatings. Thin Solid Films 455–456:650–655

[36] Fenker M, Balzer M, Kappl H, Banakh O (2005) Some properties of (Ti, Mg)N thin films deposited by reactive dc magnetron sputtering. Surf Coat Technol 200:227–231

[37] Fenker M, Balzer M, Kappl H (2006) Corrosion behaviour of decorative and wear resistant coatings on steel deposited by reactive magnetron sputtering—tests and improvements. Thin Solid Films 515:27–32

[38] Hodroj A, Chaix-Pluchery O, Steyer P, Pierson JF (2011) Oxidation resistance of decorative (Ti, Mg)N coatings deposited by hybrid cathodic arc evaporation–magnetron sputtering process. Surf Coat Technol 205:4547–4553

[39] Onder S, Kok FN, Kazmanli K, Urgen M (2013) Magnesium substituted hydroxyapatite formation on (Ti, Mg)N coatings produced by cathodic arc PVD technique. Mater Sci Eng C 33:4337–4342

[40] https://www.fiz-karlsruhe.de/de/leistungen/kristallographie/icsd.html

[41] https://www.materialsproject.org/about

[42] Hohenberg P, Kohn W (1964) Inhomogeneous electron gas. Phys Rev 136:B864–B871

[43] Kohn W, Sham LJ (1965) Self-consistent equations including exchange and correlation effects. Phys Rev 140:A1133–A1138

[44] Blöchl PE (1994) Projector augmented-wave method. Phys Rev B 50:17953–17979

[45] Kresse G, Hafner J (1993) Ab initio molecular dynamics for open-shell transition metals. Phys Rev B 48:13115–13118

[46] Kresse G, Furthmüller J (1996) Efficient iterative schemes for ab initio total-energy calculations using a plane-wave basis set. Phys Rev B 54:11169–11186

[47] Kresse G, Joubert D (1999) From ultrasoft pseudopotentials to the projector augmented-wave method. Phys Rev B 59:1758–1775

[48] Perdew JP, Burke K, Ernzerhof M (1996) Generalized gradient approximation made simple. Phys Rev Lett 77:3865–3868

[49] http://www.cif2cell.com-about.com/

[50] Ong SP, Richards WD, Jain A, Hautier G, Kocher M, Cholia S, Gunter D, Chevrier V, Persson KA, Ceder G (2013) Python materials genomics (pymatgen): a robust, open-source python library for materials analysis. Comput Mater Sci 68:314–319

[51] Armiento R et al (2012–2017) The high-throughput toolkit (httk). http://httk.openmaterialsdb.se/

[52] Momma K, Izumi F (2011) VESTA 3 for three-dimensional visualization of crystal, volumetric and morphology data. J Appl Crystallogr 44:1272–1276

[53] Wang L, Maxisch T, Ceder G (2006) Oxidation energies of transition metal oxides within the GGA + U framework. Phys Rev B 73:195107

[54] Jain A, Hautier G, Moore CJ, Ong SP, Fischer CC, Mueller T, Persson KA, Ceder G (2011) A high-throughput infrastructure for density functional theory calculations. Comput Mater Sci 50:2295–2310

[55] Monkhorst HJ, Pack JD (1976) Special points for Brillouin-zone integrations. Phys Rev B 13:5188–5192

[56] Droghetti A, Baadji N, Sanvito S (2009) MgN: a possible material for spintronic applications. Phys Rev B 80:235310

[57] Madsen GKH, Singh DJ (2006) BoltzTraP. A code for calculating band-structure dependent quantities. Comput Phys Commun 175:67–71

[58] Hunting JL, Szymanski MM, Johnson PE, Kellar CB, DiSalvo FJ (2007) The synthesis and structural characterization of the new ternary nitrides: $Ca_4TiN_4$ and $Ca_5NbN_5$. J Sol State Chem 180:31–40

[59] Bhalla AS, Guo R, Roy R (2000) The perovskite structure—a review of its role in ceramic science and technology. Mater Res Innovat 4:3–26

[60] Eklund P, Rosen J, Persson POÅ (2017) Layered ternary $M_{n+1}AX_n$ phases and their 2D derivative MXene: an overview from a thin-film perspective. J Phys D Appl Phys 50:113001

[61] Boon JW, Mac Gillavry CH (1942) The crystal structure of potassium thioferrite $KFeS_2$ and sodium thiochromite $NaCrS_2$. Recl Trav Chim Pays-Bas 61:910–920

[62] Grey IE, Steinfink H (1970) Crystal structure and properties of barium nickel sulfide, a square-pyramidal nickel (II) compound. J Am Chem Soc 92:5093–5095

[63] Jacobs H, Heckers U, Zachwieja U, Kockelmann W (2003) Lithium-Uran-Nitride: $LiUN_2$ und $Li_2UN_2$. Z Anorg Allg Chem 629:2240–2243

[64] Zhang Q-H, Wang J, Yeh C-W, Ke W-C, Liu R-S, Tang J-K, Xie M-B, Liang H-B, Su Q (2010) Structure, composition, morphology, photoluminescence and cathodoluminescence properties of $ZnGeN_2$ and $ZnGeN_2$:$Mn^{2+}$ for field emission displays. Acta Mater 58:6728–6735

[65] Seeger O, Strähle J (1994) BaCeN2, ein Bariumnitridocerat(IV) mit einer Struktur vom anti-TiP-Typ. Zeitschrift für Naturforschung B. 49:1169–1174

[66] Housecroft CE, Sharpe AG (2004) Inorganic chemistry, 2nd edn. Prentice Hall, New York

[67] Eklund P, Beckers M, Jansson U, Högberg H, Hultman L (2010) The $M_{n+1}AX_n$ phases: materials science and thin-film processing. Thin Solid Films 518:1851–1878

[68] Höglund C, Beckers M, Schell N, Borany JV, Birch J, Hultman L (2007) Topotaxial growth of Ti2AlN by solid state reaction in AlN/Ti(0001) multilayer thin films. Appl Phys Lett 90:174106

[69] Levinshtein ME, Rumyantsev SL, Shur MS (2001) Properties of advanced semiconductor materials: GaN, AIN, InN, BN, SiC, SiGe. Wiley, New York

[70] Luo X, Sullivan MB, Quek SY (2012) First-principles investigations of the atomic, electronic, and thermoelectric properties of equilibrium and strained $Bi_2Se_3$ and $Bi_2Te_3$ including van der Waals interactions. Phys Rev B 86:184111

[71] Scheidemantel TJ, Ambrosch-Draxl C, Thonhauser T, Badding JV, Sofo JO (2003) Transport coefficients from first-principles calculations. Phys Rev B 68:125210